01 Jul 2014

Mechanistic Models of Biofilm Growth in Porous Media

Priyank Jaiswal

K. Fathiya Al-Hadrami

Estella A. Atekwana
Missouri University of Science and Technology, atekwana@mst.edu

Eliot A. Atekwana
Missouri University of Science and Technology

Recommended Citation

P. Jaiswal et al., "Mechanistic Models of Biofilm Growth in Porous Media," *Journal of Geophysical Research: Biogeosciences*, vol. 119, no. 7, pp. 1418-1431, American Geophysical Union (AGU), Jul 2014.
The definitive version is available at https://doi.org/10.1002/2013JG002440

AGU PUBLICATIONS

JGR

Journal of Geophysical Research: Biogeosciences

RESEARCH ARTICLE
10.1002/2013JG002440

Key Points:
- Biofilm saturation can be predicted from ultrasonic velocities
- Morphology of Pseudomonas aeruginosa can change based on pore throat size
- In load-bearing growth form, permeability can increase at low biofilm saturation

Correspondence to:
P. Jaiswal,
priyank.jaiswal@okstate.edu

Citation:
Jaiswal, P., F. Al-Hadrami, E. A. Atekwana, and E. A. Atekwana (2014), Mechanistic models of biofilm growth in porous media, *J. Geophys. Res. Biogeosci.*, *119*, 1418–1431, doi:10.1002/2013JG002440.

Received 16 JUL 2013
Accepted 2 JUL 2014
Accepted article online 7 JUL 2014
Published online 25 JUL 2014

Mechanistic models of biofilm growth in porous media

Priyank Jaiswal[1], Fathiya Al-Hadrami[1], Estella A. Atekwana[1], and Eliot A. Atekwana[1]

[1]Boone Pickens School of Geology, Oklahoma State University, Stillwater, Oklahoma, USA

Abstract Nondestructive acoustics methods can be used to monitor in situ biofilm growth in porous media. In practice, however, acoustic methods remain underutilized due to the lack of models that can translate acoustic data into rock properties in the context of biofilm. In this paper we present mechanistic models of biofilm growth in porous media. The models are used to quantitatively interpret arrival times and amplitudes recorded in the 29 day long Davis et al. (2010) physical scale biostimulation experiment in terms of biofilm morphologies and saturation. The model pivots on addressing the sediment elastic behavior using the lower Hashin-Shtrikman bounds for grain mixing and Gassmann substitution for fluid saturation. The time-lapse *P* wave velocity (V_P; a function of arrival times) is explained by a combination of two rock models (morphologies); "load bearing" which assumes the biofilm as an additional mineral in the rock matrix and "pore filling" which assumes the biofilm as an additional fluid phase in the pores. The time-lapse attenuation (Q_P^{-1}; a function of amplitudes), on the other hand, can be explained adequately in two ways; first, through squirt flow where energy is lost from relative motion between rock matrix and pore fluid, and second, through an empirical function of porosity (ϕ), permeability (κ), and grain size. The squirt flow model-fitting results in higher internal ϕ (7% versus 5%) and more oblate pores (0.33 versus 0.67 aspect ratio) for the load-bearing morphology versus the pore-filling morphology. The empirical model-fitting results in up to 10% increase in κ at the initial stages of the load-bearing morphology. The two morphologies which exhibit distinct mechanical and hydraulic behavior could be a function of pore throat size. The biofilm mechanistic models developed in this study can be used for the interpretation of seismic data critical for the evaluation of biobarriers in bioremediation, microbial enhanced oil recovery, and CO_2 sequestration.

1. Introduction

Formation of biofilms is a predominant way of life for most microorganisms in the environment. Biofilms comprise dominantly of extracellular polysaccharides (EPS), which is a gel-type material playing a vital role in attachment of microbial cells to growth surfaces [*Hall-Stoodley et al*., 2004; *Lear and Lewis*, 2012]. In both natural and bioengineered systems, the formation of biofilms has been linked to pore throat clogging [*Drescher et al*., 2013] leading to the alteration of sediment physical [*Taylor and Jaffé*, 1990], fluid transport [*Abdel-Aal et al*., 2009], and sediment mechanical and hydrodynamic properties [*Rosenzweig et al*., 2013]. Biofilms have been found to decrease porosity (ϕ) by ~50%–90% and permeability (κ) by ~95%–99% [*Cunningham et al*., 1991]. The ability to monitor microbial growth and manage artificial and natural bioclogging is essential in many applications related to soil engineering [*DeJong et al*., 2010], groundwater remediation [*Kasi et al*., 2011], CO_2 sequestration [*Mitchell et al*., 2010], and microbial enhanced oil recovery (MEOR) [*Lazar et al*., 2007].

In situ imaging of bioinduced sediment alterations are critical in understanding microbial growth habits. In laboratory experiments, biofilm formation and development have been investigated using confocal laser scanning microscopy [*Lawrence and Neu*, 1999], epifluorescent microscopy [*Garcia-Betancur et al*., 2012], plate counting and column tracer tests [*Seifert and Engesgaard*, 2007], synchrotron-based X-ray-computed microtomography [*Davit et al*., 2011], and nuclear magnetic resonance [*Manz et al*., 2003; *Vogt et al*., 2013]. In field settings, pump tests or slug tests designed to evaluate the change in hydraulic conductivity are used to infer the presence of bioclogging indicative of the presence of biofilms.

Both laboratory- and field-based experiments unequivocally show that biofilm growth changes the physical and chemical environment of porous media. Only a limited number of models exist to describe these changes. Of these, many treat the biofilms as a complex fluid [*Wilking et al*., 2011]. A more realistic approach could be to incorporate the biofilms in the rock as a solid phase, but this requires mechanical data such

Table 1. Biofilm Mechanical Properties Young's Moduli (GPa)

Source
Nishi et al. [1990]
Hsieh et al. [2008]
Tajima et al. [1995]
Stoodley et al. [2002]
Konhauser and Gingras [2007]
Stoodley et al. [1998]
Guhados et al. [2005]
Aggarwal and Hozalski [2010]

as Young moduli (Y), Poisson's ratio (v), and density (ρ), as well as information on biofilm microstructure. Such data are not only limited but also when available have a wide range (e.g., Table 1), probably due to heterogeneity of the biofilms as well as the lack of standardized testing methods.

Insight into processes such as bioclogging can be obtained through continuous monitoring of microbial growth, but the key is to achieve this without interfering with the growth itself. Acoustic methods at ultrasonic frequency range can serve as an effective monitoring tool [*Atekwana and Slater*, 2009; *Davis et al*., 2010; *Kwon and Ajo-Franklin*, 2013; *Williams et al*., 2005]. The greatest advantage is their nondestructive and noninvasive nature. A major limitation, which also keeps this method largely underutilized, is a lack of models that can be used to translate acoustic data into rock properties in biofilm environments. This paper is a pioneering attempt to develop mechanistic models of biofilm growth in unconsolidated sediments. The models are developed and used to quantitatively interpret, group arrival times, and amplitude of the dominant frequency (0.4 MHz) from the *Davis et al.* [2010] physical scale experiment.

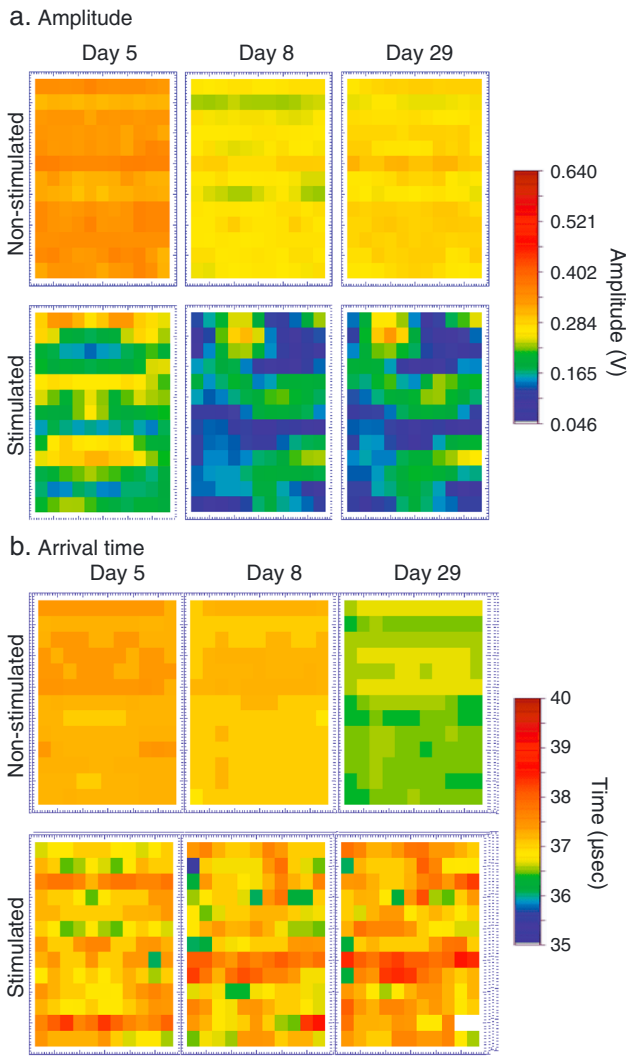

Figure 1. Two-dimensional map of the (a) compressional wave amplitude and (b) arrival time for stimulated and control columns for days 5, 8, and 29 from the *Davis et al.* [2010] experiment. The stimulated column clearly shows perturbations in both amplitudes and arrival times.

Davis et al. [2010] recorded compressional waves and complex conductivity data during 29 days of stimulated microbial growth in porous media. In their experiment, two (identical) acoustic wave and complex conductivity measurement sample columns were constructed one of which was biostimulated. Waveforms were recorded in both columns every 3–5 days. The arrival time and amplitude data used in this paper were extracted from the waveforms using *Li and Pyrak-Nolte* [1998] method. Over the 29 days, the amplitudes and arrival times from the nonbiostimulated column remained relatively uniform while data from the biostimulated sample exhibited a high degree of spatial variability, with portions of the sample exhibiting up to 80% decrease in amplitudes (Figure 1). Between days 5 and 7, both amplitudes and arrival times changed significantly in the biostimulated column. The imaginary conductivity, which *Davis et al.* [2010] interpreted in terms of biofilm stages, also peaked by day 7; the peak was interpreted to represent maximum biofilm thickness and the decrease was suggested to be related to cell death or detachment.

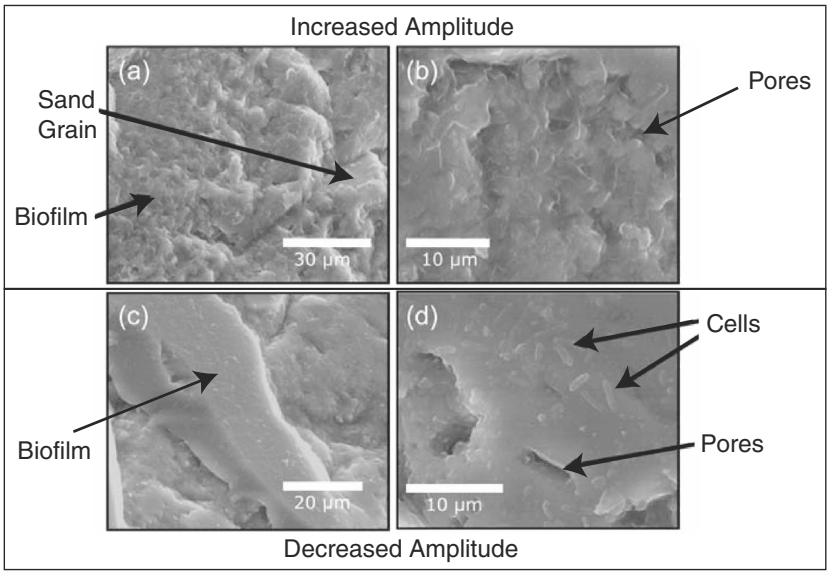

Figure 2. Environmental scanning electron microscope (ESEM) images from *Davis et al*. [2010] experiment. (a and b) From an area of increased amplitude and (c and d) from an area of decreased amplitude. Biofilms from the increased amplitude zone appear to be vuggier.

Environmental scanning electron microscope (ESEM) imaging at the end of the *Davis et al*. [2010] experiment confirmed that there was an apparent difference in the morphology of attached biomass between regions of increased and decreased attenuation (Figure 2). This begs the question why two distinct morphologies formed in an otherwise uniform growth media? We investigate this question through mechanistic models that are based on gas hydrate growth in unconsolidated marine sediments [*Dvorkin and Nur*, 1996]. We postulate that from a modeling perspective, growth of gas hydrate is analogous to biofilm growth with the caveat that while hydrate precipitate from pore fluids [*Sloan and Koh*, 2008], biofilms originate at the surface of the sediment grains. Similar to hydrate, our mechanistic models also pivots on being able to address the elastic behavior of sediments using the Hertz-Mindilin theory [*Mindlin*, 1949] for grain mixing and the Gassmann substitution for fluid saturation [*Gassmann*, 1951].

2. Experimental Setup

We provide a brief description of the experimental setup. More details can be obtained from *Davis et al*. [2010]. *Davis et al*. [2010] fabricated rectangular sample columns that measured 102 mm × 51 mm by 254 mm (width × depth × height) from 3.2 mm thick clear acrylic (Figure 3). Two sets of experimental columns were constructed, one each for control (nonstimulated) and stimulated. All columns were wet packed with silica sand saturated with sterile 25% BH (Bushnell Haas; Becton Dickinson) nutrient broth. One set of columns (one electrical and one acoustic) was inoculated by saturating with 25% BH broth, 30 mM glucose, *Pseudomonas aeruginosa* bacterial culture, and 30 mg/mL Gentamicin antibiotic. The fluid in the columns remained stagnant during this experiment, and the columns were not fed with additional nutrients.

The acoustic imaging system consisted of two water-coupled plane wave transducers as source and receiver, computer-controlled linear actuators (Newport 850-B4 and Motion Master 2000), a high-voltage pulse generator (Panametrics PR1500), and an oscilloscope (Lecroy 9314L). In the experiment, waveforms were recorded over a two-dimensional region. Linear actuators were used to move the source and receiver in increments of 5 mm over the 60 mm by 70 mm acoustic scan region. An oscilloscope recorded and digitized the transmitted signals at each point in the scan region. In total, nine sets of ultrasonic waveforms scans were recorded. Individual sets of scans comprised measurements at 168 locations in a rectangular matrix of 14 × 16 cells, each cell measuring 5 × 5 mm^2. Although the experimental data were not collected at a uniform temporal interval, the measurements adequately captured biofilm inception, growth, and decay (Figure 1).

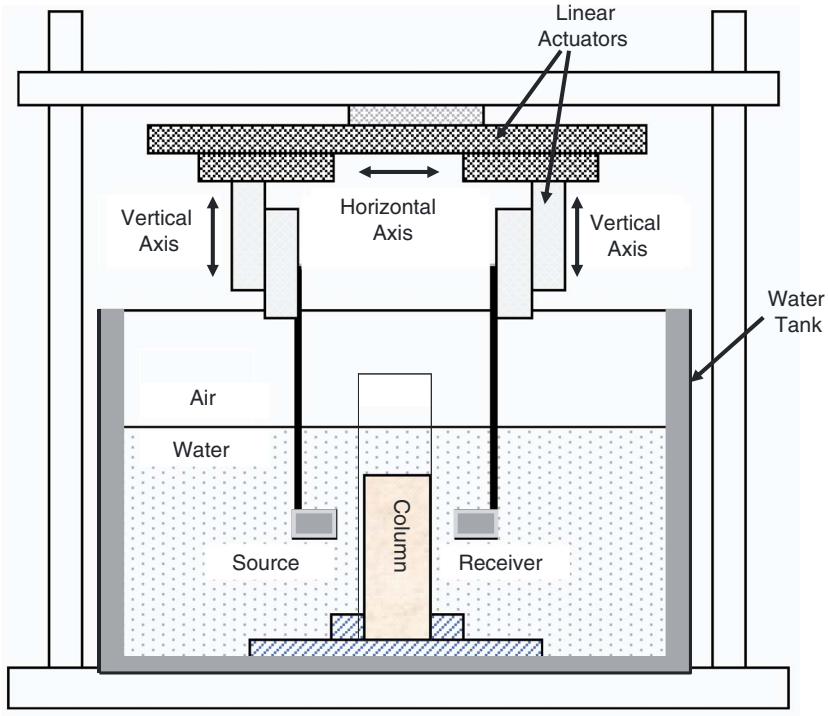

Figure 3. Cartoon of the acoustic imaging system used in the *Davis et al.* [2010] experiment.

3. Model Formulation

The ultrasonic waves in the *Davis et al.* [2010] experiment traveled through three media between source and receiver—water, Pyrex enclosure, and sediments. To discount the effect of Pyrex (3.2 mm on either side) and water (5 mm or either side), we reduce the arrival times by 7.7 ms and convert the results to compressional wave velocity (V_P) assuming straight rays and a sediment thickness of 45 mm. Figure 4 is a display of the V_P sorted according to average V_P (for all days) increasing from left to right. We interpret the onset of biofilm formation on day 3 based on the V_P decreases in all the cells. From Day 5 onward, two distinct V_P trends can be observed, predominantly decreasing, e.g., in cells 1–20 and predominantly

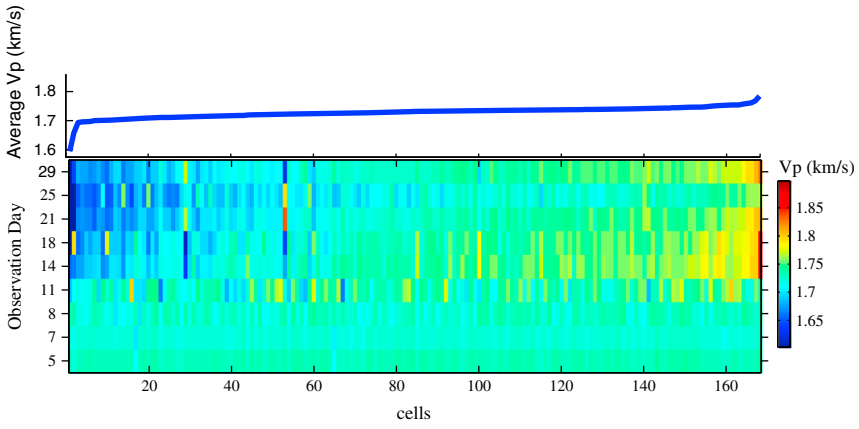

Figure 4. Time-lapse velocity. V_P change within the 168 cells over 29 days of observation. The data are plotted based on the averaged V_P in each cell node. The results show a general decrease in V_P on day 5. Two dominant trends are observed thereafter: (1) generally decreasing (e.g., cells 0–20) and (2) general increase (e.g., cells 150–168). The time-lapse V_P trend in the remaining nodes can be described by a combination of increasing and decreasing trends.

increasing, e.g., in cells 150–168. Time-lapse V_P in the remaining cells can be decomposed in terms of the two trends. It is possible that the two trends are due to development of two distinct biofilm morphologies.

The V_P of a system depends on its elastic moduli. Therefore, to model the time-lapse V_P changes, first, the time-lapse changes in elastic moduli due to biofilm growth have to be estimated. In the *Dvorkin and Nur* [1996] model, elastic moduli are computed by separately computing the moduli of constituent dry-sediments and pore fluid, followed by merging both moduli using the Gassmann's substitution. While this approach works well in siliciclastic rocks at low seismic frequencies [*Nolen-Hoeksema*, 2000; *Xu and White*, 1995], based on the inherent assumptions of the Gassman's substitution [*Hofmann*, 2006], it could be argued that it may not be appropriate for use at ultrasonic frequencies. *Mavko and Nolen-Hoeksema* [1994] and *Adam et al.* [2009] have shown that Gassmann's substitution can remain valid at ultrasonic frequencies if the rock does not have a strong fabric or oriented cracks. Since the *Davis et al.* [2010] setup comprises sand grains that are packed together without a preferred orientation; the Gassmann's assumptions are assumed to be applicable.

The elastic moduli of a porous sediment refer to its resistance against deformation under seismic stress. The modulus of a monomineral solid is a function of its porosity (ϕ). Generally speaking, higher ϕ implies lower moduli (at higher ϕ, the material deforms more easily). For multimineral solids, such as naturally occurring rocks, expression of elastic moduli is complex. The elastic moduli are at their maximum and minimum, respectively, at zero (φ_0) and critical porosity (φ_c; the limit at which the mineral grains become free floating). Between φ_0 and φ_c, moduli can change in many ways depending on the grain arrangement and consolidation state of the rock [*Mavko et al.*, 2009]. *Dvorkin and Nur* [1996] showed that for unconsolidated sediments, such as in *Davis et al.* [2010], the modified lower Hashin-Shtrikman bounds best explains the dry rock moduli change.

Assuming a homogenous background of quartz grains that are uncemented, spherical, and randomly packed, the bulk (K) and shear (G) moduli at one endpoint, ϕ_c, can be expressed by the Hertz-Mindlin theory:

$$K_{\phi_c} = \left[\frac{n^2(1-\phi_c)^2G^2}{18\pi^2(1-\nu)^2}P\right]^{\frac{1}{3}}, \quad G_{\phi_c} = \frac{5-4\nu}{5(2-\nu)}\left[\frac{3n^2(1-\phi_c)^2G^2}{2\pi^2(1-\nu)^2}P\right]^{\frac{1}{3}}. \tag{1}$$

In equation (1), n is the average number of contacts per grain (9 in this paper). P is the differential pressure, and v and G are the Poisson's ratio and shear modulus of the solid phase. At the other endpoint, ϕ_0, the elastic moduli for two or more mineral phases can be calculated using the Hill's average [*Hill*, 1952] and mass balance as follows:

$$K_{\phi_0} = 0.5\cdot\left[\sum_{i=1}^{m} f_i K_i + \left(\sum_{i=1}^{m} f_i/K_i\right)^{-1}\right]; \quad G_{\phi_0} = 0.5\cdot\left[\sum_{i=1}^{m} f_i G_i + \left(\sum_{i=1}^{m} f_i/G_i\right)^{-1}\right]; \quad \rho_{\phi_0} = \sum_{i=1}^{m} f_i\rho_i \tag{2}$$

In equation (2), is the number of the mineral components in the rock matrix; is the volumetric fraction of the th matrix mineral component; and K_i, G_i, and ρ_i are the bulk moduli, shear moduli, and density of the th matrix mineral component, respectively. Depending on the geometric configuration of the mineral constituents, the actual K and G can be higher or lower than Hill's average; however, it is a reasonable estimate for randomly arranged solid mineral constituents.

For the dry frame for $\phi < \phi_c$ bulk and shear moduli (K_{dry} and G_{dry}, respectively) using the modified lower Hashin-Shtrikman bound can be expressed as follows:

$$K_{\text{Dry}} = \left[\frac{\phi/\phi_c}{K_{\phi_c}+\frac{4}{3}G_{\phi_c}} + \frac{1-\phi/\phi_c}{K_{\phi_0}+\frac{4}{3}G_{\phi_c}}\right]^{-1} - \frac{4}{3}G_{\phi_c}; \quad G_{\text{Dry}} = \left[\frac{\phi/\phi_c}{G_{\phi_c}+Z} + \frac{1-\phi/\phi_c}{G_{\phi 0}+Z}\right]^{-1} - Z; \tag{3}$$

$$Z = \frac{G_{\phi_c}}{6}\left(\frac{9K_{\phi_c}+G_{\phi_c}}{K_{\phi_c}+G_{\phi_c}}\right)$$

The bulk modulus (K_f) and density (ρ_f) of the pore fluid can be expressed as follows:

$$K_f = \sum_{i=1}^{p}\left[\frac{S_{fi}}{K_{fi}}\right]^{-1}; \rho_f = \sum_{i=1}^{p} S_{fi}\rho_{fi}; \sum_{i=1}^{p} S_i = 1 \tag{4}$$

In equation (4), p is the number of fluid components, K_{fi}, ρ_{fi}, and S_i are bulk modulus, density, and saturation of the ith fluid component present in the pores. Note that fluids do not have shear modulus. The bulk modulus of saturated rock (K_{sat}) can be expressed using the Gassmann's substitution as follows:

$$K_{Sat} = K_{\phi_0} \frac{\phi K_{Dry} - (1+\phi) K_f K_{Dry}/K_{\phi_0} + K_f}{(1-\phi) K_f + \phi K_{\phi_0} - K_f K_{Dry}/K_{\phi_0}} \tag{5}$$

The shear modulus of saturated rock (G_{Sat}) remains the same as that of the dry rock: $G_{Sat} = G_{Dry}$; and the bulk density (ρ_b) of the saturated rock is the following:

$$\rho_b = (1-\phi)\rho_{\phi_0} + \phi\rho_f, \tag{6}$$

Values for K_f in equation (5) and ρ_f in equation (6) can be computed using the *Batzle and Wang* [1992] method. Finally, V_P can be expressed as follows:

$$V_p = \sqrt{(K_{Sat} + {}^4/_3 G_{Sat})/\rho_b} \tag{7}$$

On a related note, the above model can also predict the S wave velocity, $V_S = \sqrt{G_{Sat}/\rho_b}$ which if experimentally available, can be used as an additional model constrain.

For modeling the mixture of biofilm, sand, and water (constituents of the *Davis et al*. [2010] experiment), individual K, G, and ρ of all the three components are required. While the K, G, and ρ of sand and water are well known, that of the biofilm is not. Therefore, for modeling purposes, we have made a few simplistic assumptions. The EPS of *P. aeruginosa* dominantly consists of alginate which is an anionic polysaccharide. In nature, instead of alginate, some bacteria generate polysaccharide in the form of cellulose. Although the chemistry of alginate and cellulose are different, due to the similarity in the way the two polysaccharides are constructed, we suggest that it is fair to substitute the mechanical properties of one for the other. In this paper, we use Y of hemicellulose (5–8 GPa *Gibson* [2012]), which is an amorphous from of cellulose. For this form we hypothesize that v is nearly zero, relating biofilm to extremely unconsolidated sediments or a sponge. The biofilm ρ appears to be dependent on its (internal) ϕ [*Rabah and Dahab*, 2004; *Zhang and Bishop*, 1994]. We choose a value of 1.5 g/cm^3 which is representative of both hemicelluloid [*Ehrnrooth*, 1984] as well as the dry EPS [*Talukdar et al*., 1996].

Like gas hydrates, we propose that the biofilms can be introduced in the unconsolidated sediments as a part of the matrix or as a part of the pore fluid. In the *Dvorkin and Nur* [1996] model, introduction of hydrate in the matrix assumes that it acts like an additional mineral grain which participates in the transfer of seismic stress (load-bearing form). Introduction of hydrate in fluids (pore-filling form), on the other hand, only requires the bulk modulus of the original pore fluid to be proportionately replaced by bulk modulus of the hydrate. We acknowledge that unlike hydrates, biofilms do not precipitate from pore fluid, but rather grow on a solid surface.

Klausen et al. [2003a, 2003b] show that the biofilms first originate on the surface of the mineral grains and then spread laterally. We conceive that at the initial stages, developing biofilms may not bridge mineral grains (Figure 5a), and hence, their presence in the model can be approximated by the pore-filling form. With time, we postulate that the growth style will be a function of pore throat size. The load-bearing and pore-filling forms in our model are intended to be, respectively, representative of growth under restricted and unrestricted accommodation space. When vertical accommodation space is small, e.g., between two mineral grains, after spreading along the grain surface (Figure 5b), the biofilm bridges the gap between two mineral grains (Figure 5c). On the other hand, when the vertical accommodation space is relatively unrestricted, e.g., in the pore spaces between three or more grains, the biofilm can continue to grow vertically (Figure 5c). This could potentially create two very different morphologies, possibly those that were observed in the *Davis et al*. [2010] experiment.

4. Model Validation

The first step in modeling is to determine the initial porosity, ϕ_i. On day 1, assuming biofilm saturation (S_{bf}) to be zero, the V_P is 1.734 ± 0.0051 km/s. For this V_P, with water as pore fluid, the *Dvorkin and Nur* [1996] model yields $\phi_i = 37.85$. In the next step, to show the effect of including biofilms in the sand pack in the load-

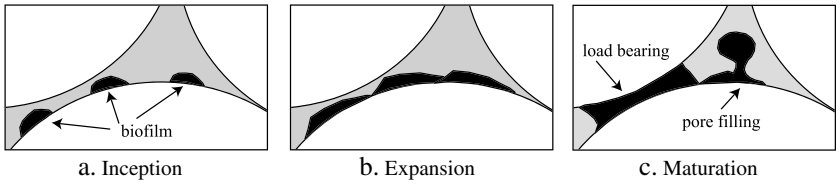

Figure 5. Biofilm growth styles. (a) Inception. Biofilm growth is initiated on a grain surface. (b) Expansion. Biofilm expand both vertically and horizontally. (c) Maturation. Biofilm continues to grow into the pore spaces and due to a lack of accommodation space between mineral grains, they expand along the surface which results in their interconnection. At this stage, biofilms act like an additional mineral grain in load-bearing form or an additional fluid component in the pore-filling form.

bearing and pore-filling forms, we present a parametric test for a range of biofilm v (Figure 6a) and Y (Figure 6b). When S_{bf} is increased in the load-bearing form, ϕ in equation (3) decreases as $\phi_i(1 - S_{bf})$. Decreasing ϕ will increase the system's V_p. In our case, low biofilm Y counters this increase (solid lines; Figure 6). On the other hand, when S_{bf} increases in the pore-filling mode, ϕ in equation (3) remains unchanged. The K and G of the dry matrix remain unchanged but fluid ρ increases while its K decreases (equation (4)). This in turn reduces the V_p of the system (solid dots; Figure 6). In the absence of firm experimental data, $v = 0$ and $Y = 6$ GPa could represent reasonable values of biofilm mechanical properties.

Davis et al. [2010] also reported a decrease in pH value from 7.0 on day 1 to ~4.4 on day 26, implying that the acidity of the system increased with microbial growth and biofilm formation and development. A possible reason for lowering of the pH is the production of $CO_{2(g)}$, which dissolves in the pore water as the system equilibrates [*Le Chatelier*, 1998]: $CO_{2(aq)} + H_2O \leftrightarrow H_2CO_3 \leftrightarrow HCO_3^-$. As opposed to the dissolved form, gas can significantly lower V_P when present in the bubble form. Bubbles are typically formed when gas concentration exceeds its solubility. To examine the presence of gas bubbles, the partial pressure of CO_2 needs to be expressed as a function of pH (Henry's law) [*Smith and Harvey*, 2007]:

$$\log P_{CO_2} = -\mathrm{pH} + \log\left(\frac{\gamma_{HCO_3^{-1}} M_{HCO_3^{-1}}}{K_1 K_{CO_2}}\right) \tag{8}$$

In equation (8), γ and M are the activity coefficient and the molarity, respectively. K_1 is the first dissociation constant of H_2CO_3 and K_{CO_2} is Henry's law constant for CO_2; both values are corrected for the sample temperature (T). The resulting P_{CO_2} is presented in Table 2. Even at maximum P_{CO_2} (Table 2), CO_2 concentration is less than its solubility (1.45 g/L; 5.73 MPa), no bubbles are therefore expected in the *Davis et al.* [2010] experiment (the authors also reported that they did not observe any bubble formation). Dissolved CO_2 changes fluid properties in equation (4). In our case, this results in a reduction of V_P by up to 0.002 km/s, which

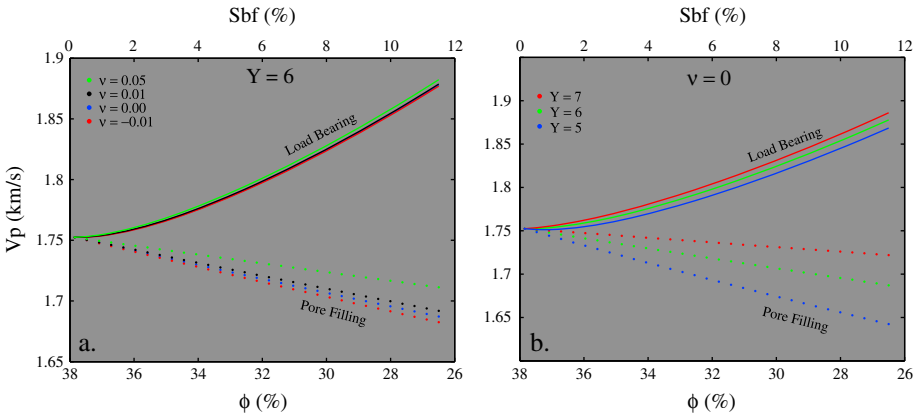

Figure 6. Velocity versus porosity/biofilm saturation. Decreasing porosity is proportional to increasing biofilm saturation. Synthetic modeling shows that V_P increases when biofilm is introduced in load-bearing form (blue line) and V_P decreases if biofilm is introduced in the pore-filling form (red line).

Table 2. P_{CO2} in kPa

Alkalinity	pH = 7	pH = 5	pH = 4.5	pH = 4
50	0.0063	1.288	2.0711	7.005
100	0.01245	2.5345	4.0439	13.292
150	0.01868	3.7644	5.997	19.552

is within the standard deviation of the V_P in the absence of biofilms and therefore inconsequential to our model.

The V_p in the *Davis et al*. [2010] experiment continually changes in every cell throughout the duration of the experiment (Figure 4); some cells exhibit more change on certain days compared to others. If cells with a positive V_p change are categorized as "load bearing" and cells with a negative V_p change are categorized as "pore filling," Figure 6 can be used to map V_P perturbations to S_{bf}. The underlying assumption is that S_{bf} monotonically increases in all cells. This approach provides flexibility to change the growth forms (from pore filling to load bearing or vice versa) in estimating S_{bf} at individual cells. However, it has a drawback. It assumes mutually exclusive growth forms. Our model uses a single growth form at an individual cell between two observations days which is based on the net V_P change. Since the two growth forms have opposing effect on the V_p (Figure 6), our approach yields a very conservative S_{bf} estimate.

Mapping positive V_p perturbation as an increase in the load-bearing form (Figure 7a) and negative perturbations as an increase in the pore-filling form (Figure 7b) shows an overall ϕ decreased of 10%, with as much as 15% decrease at a few selected locations (Figure 7c). This value is consistent with data obtained in a bioclogging experiment by *Abdel-Aal et al*. [2010] using *P. aeruginosa* culture and sands. Arranging cells based on average V_P (Figure 4) aids in the visualization of our results. In Figure 7a, cells with dominant load-bearing form are numbered 140 and higher. Similarly, cells with dominant pore-filling form are numbered 60 and lower. In cells 60–140, biofilm grows in equally in both forms.

As opposed to the traveltime/V_P which increased and decreased throughout the experiment, the peak-to-peak amplitudes (A^{P2P}) generally decreased with time [*Davis et al*., 2010]. A^{P2P} changes can be related to seismic attenuation which is the loss of seismic energy in a single cycle [*Batzle et al*., 2005]. Mathematically, it can be represented by the inverse of a dimensionless "quality factor" Q_P as follows:

$$\frac{1}{Q_P} = -\frac{\delta A^{P2P}}{\pi A_i^{P2P}} \tag{9}$$

In equation (9), A^{P2P} is current and A_i^{P2P} is peak-to-peak amplitudes on the first day. It is intuitively expected that biofilm growth will increase attenuation. However, the *Davis et al*. [2010] experiment has an exception; a display of $\pi.Q_P^{-1}$ computed using equation (9), suggests that the attenuation decreases in cells 150–165 on day 7 (Figure 7d). A comparison of Figures 7a and 7d suggests that this decrease could be related to the early stages of the load-bearing form. Figure 7d further shows that attenuation increases most rapidly in cells 5–35. A comparison of Figures 7b and 7d suggests that increased attenuation could be related to the pore-filling mode.

Attenuation is a complex phenomenon which depends on a multitude of factors such as frequency, grain shape and size, fracture density and aspect ratio, as well as fluid saturation and viscosity. As a result, models for attenuation are generally more difficult to formulate than they are for V_P; more so for biofilms due to a scarcity of relevant data. Here we have attempted to model the observed peak-to-peak amplitude changes in two ways. First, using the "squirt flow" theory [*Mavko and Nur*, 1979] which takes the biofilm texture into account and second, using an empirical model that takes medium bulk properties into account.

Attenuation through squirt flow, as amplitude decay in porous media, implies heat loss due to relative motion between solid (dry matrix) and liquids (pore fluid). The relative motion is higher in pores that are "soft," i.e., that get easily deformed under seismic stress. By definition, the remaining "stiff" pores do not contribute to squirt flow. In the high-frequency limit, i.e., when pore pressure distribution in the rock does not equilibrate within the wave half-cycle, *Gurevich et al*. [2010] formulated Q_P^{-1} as a function of P and frequency (f) as follows:

$$\frac{1}{Q_P(p,f)} = \frac{\alpha\phi^*(P)K_{dry}}{\sqrt{3\pi f\eta K_f}} \tag{10}$$

In equation (10), α is the pore aspect ratio (ratio of radius and length), ϕ^* is the volume of soft pores, and η is the viscosity of the fluid that squirts in and out of the soft pores. For modeling attenuation using squirt

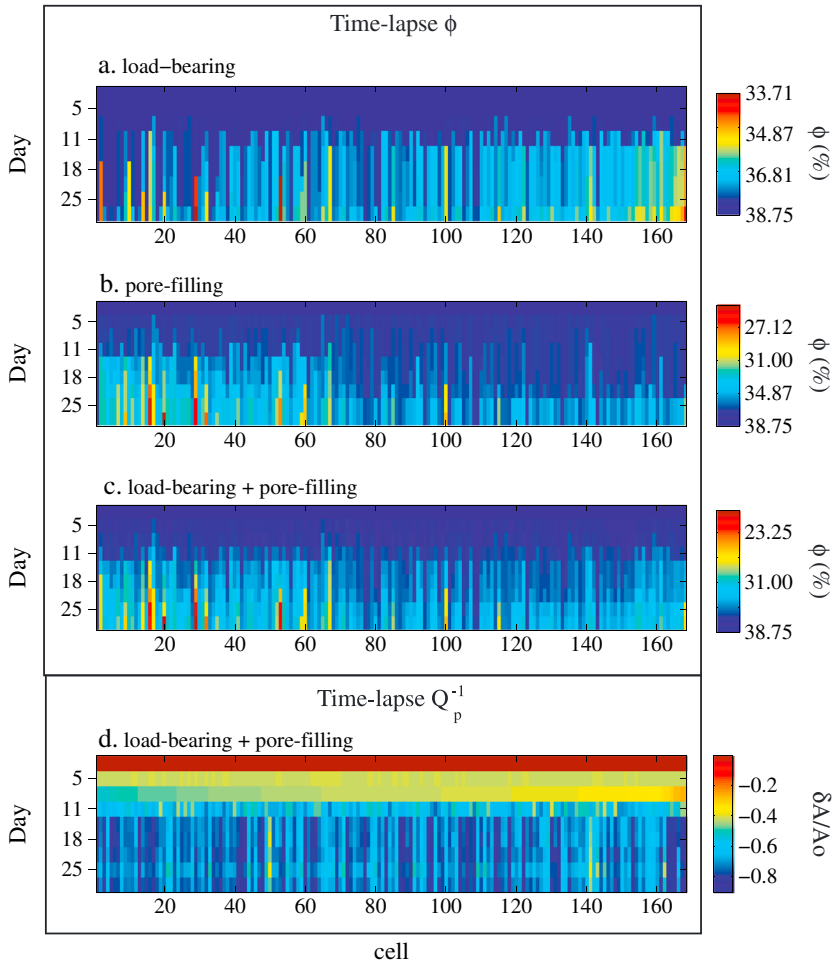

Figure 7. Time-lapse porosity and attenuation. (a) Porosity decreases due to growth of biofilm in load-bearing mode. (b) Porosity decreases due to growth of biofilm in pore-filling mode. (c) Total decrease in porosity. (d) Time-lapse amplitude change as an indication of attenuation (see text for details). Attenuation consistently increases at all model locations except in cells 130–165 on day 3. In cells 130–165, biofilms appear to have a load-bearing growth style.

flow, we make some simplistic but logical and intuitive assumptions. First, we assume that the pore fluid is a colloid comprising microbial cells suspended in water and use the exponential law proposed by *Cheng et al.* [2002] for colloidal η:

$$\eta = \eta_0 e^{\left(aS_{bf}^{*}+b\right)} \tag{11}$$

In equation (11), S_{bf}^{*} is the volume fraction of biofilm cells suspended in the pore water (assumed to be detached from the original framework), a and b are model constants, and η_0 is the viscosity of water in the absence of any suspensions. In line with *Davis et al.* [2010], we use the complex conductivity [*Davis et al.*, 2010, Figure 12a] as a proxy for biofilm detachment assuming that the absolute changes in the complex conductivity are linearly proportional to the fraction of detached biofilm from the solid surface. The complex conductivity curve in *Davis et al.* [2010] is bell shaped [*Davis et al.*, 2010, Figure 12a] begins at a base value, peaks on the seventh day of observation and exponentially declines thereafter to its starting base value. We approximate S_{bf}^{*} with $(1-c)*S_{bf}^{t}$, where S_{bf}^{t} is the total biofilm saturation (Figure 7c), c is a detachment array ranging between 0.01 (implying 1% of S_{bf}^{t} is in the detached state) and 0.99 (implying 99% of S_{bf}^{t} is in the detached state) such that $c*S_{bf}^{t}$ imitates the complex conductivity.

In the *Davis et al.* [2010] experiment, attenuation is not limited to the biostimulated column. Even in the nonbiostimulated column, the source wavelet gets attenuated, and over 29 days, the attenuation

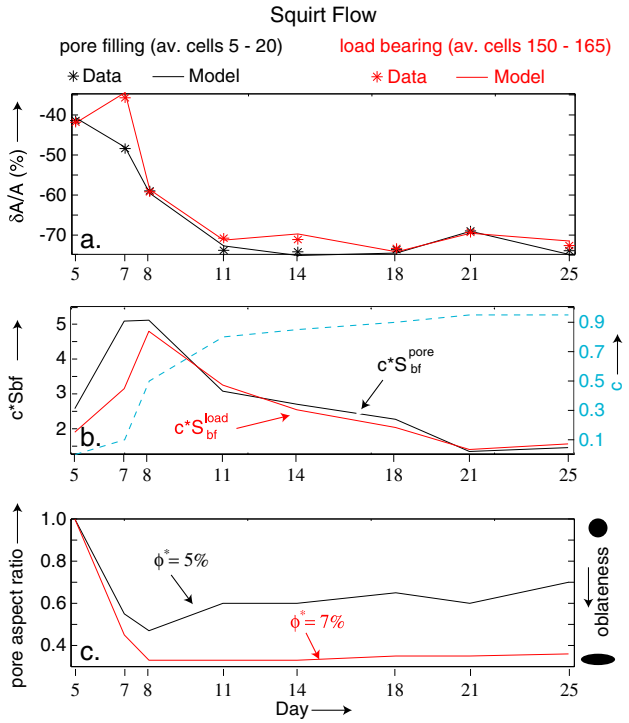

Figure 8. Squirt flow attenuation model. (a) Black and red stars, respectively, represent averaged attenuation observed from days 2–9 from cells 5–15 and 150–165. Black and red lines represent attenuation predicted using equation (10). (b) Array c^*S_{bf} for pore-filling and load-bearing forms are shown in black and red lines, respectively. S_{bf} for their respective forms are from Figure 3 and ϕ^* is indicated. Detachment array c is shown in dashed blue line. (c) The time-lapse evolution in pore shape for pore-filling and load-bearing forms is shown in black and red lines, respectively. Load-bearing form has higher ϕ^* and more oblate pores.

characteristics changes, albeit modestly (<5%) as compared to the biostimulated column (up to 80%). Our explanation is as follows. Squirt flow occurs in the sand pack in both biostimulated and nonbiostimulated columns. The internal settling of the pack over time is expected to slightly change the attenuation character, as observed in the *Davis et al.* [2010] experiment. We expect the pores within the biofilm to be "softer" than the sand pack pores. In which case, the loss of energy could be higher as pore fluid squirt in-and-out of the biofilm EPS as compared to pores of the sand pack. Thus, S^t_{bf} can strongly influence attenuation.

In equation (10), ϕ^* can be assumed as the biofilm porosity; K_{dry} and K_f can be obtained from equations (3) and (4); the differential pressure (ambient conditions) can be assumed constant throughout the experiment and f is the dominant frequency. Rather than modeling Q_P^{-1} at every cell, we compare and contrast model parameters in dominantly pore-filling form (cells 5–35; Figure 7b) versus dominantly load-bearing form (cells 150–165; Figure 7a). Figure 8a is a plot of $\frac{\delta A^{P2P}}{A_i^{P2P}}$ versus observation days. Black and red stars in Figure 8a indicate average $\frac{\delta A^{P2P}}{\pi A_i^{P2P}}$ from cells 5–25 and 150–165, respectively. Black and red lines in Figure 8a are model predictions using equations (9) and (10). The arrays $c^*S_{bf}^{pore}$ and $c^*S_{bf}^{load}$ corresponding to pore-filling and load-bearing forms are shown in Figure 8b in black and red, respectively (S_{bf}^{pore} and S_{bf}^{load} are from Figures 7a and 7b, respectively), and array c is shown in dashed blue line. Array α for pore-filling and load-bearing forms is shown in Figure 8c in black and red lines, respectively. Based upon model fitting (Figure 8a), the squirt flow requires biofilms in the load-bearing form to have (a) more oblate pores and (b) higher ϕ^* (Figure 8c).

Attenuation can also be explained using an empirical model. For a plane wave, the amplitude decay can be expressed as $A(x) = A_0\, e^{-ax}$, where x is the travel path and a is a system-dependent constant defined as follows [*Boadu*, 1997]:

$$a = a_0 + a_1\phi + a_2\kappa + a_3 D \tag{12}$$

In equation (12), D is the mean grain size (mm) and a_0 through a_3 are system-dependent constants. Equations (9) and (12) can be combined as follows:

$$\frac{1}{Q_P} = -\frac{\delta A}{\pi A_0} = -\frac{1}{\pi}\left(1 - e^{(a_0 + a_1\phi + a_2\kappa + a_3 D)x}\right) \tag{13}$$

In our case, for equation (13), we can assume that D remains constant, x is the thickness of the sedimentary column (51 mm), and obtain the time-lapse ϕ (Figure 4c). With an initial permeability $\kappa_i = 5\ D$ (corresponding to $\phi_i = 38.75\%$ [*Costa*, 2006]), modeling Q_P^{-1} from cells 5–25 and 150–165 yields two κ arrays corresponding to

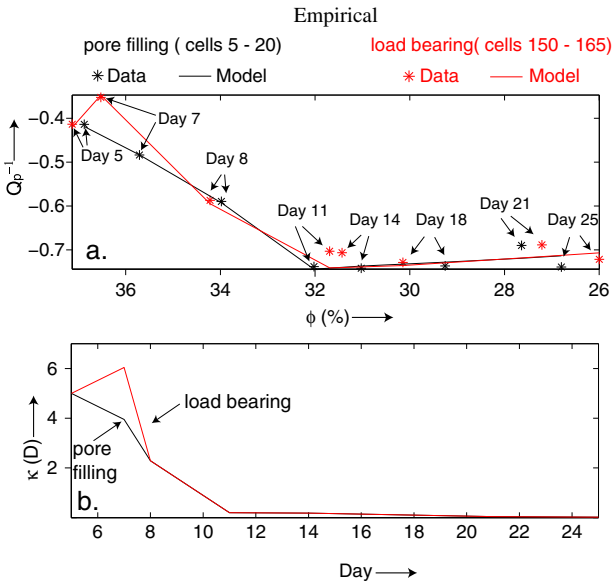

Figure 9. Empirical attenuation model. (a) Attenuation as a function of bulk ϕ. Black and red stars have the same meaning as in Figure 8a. Attenuation for pore-filling (black) and load-bearing (red) forms using equation (13). (b) Average ϕ for pore-filling (cells 5–15; black) and load-bearing (cells 150–165; red) forms. While bulk ϕ decreases, in load-bearing form, local ϕ increases at low (~2%) saturation.

pore-filling and load-bearing forms (Figure 9). As intuitively expected, Figure 9a shows that in general, deceasing κ increases Q_P^{-1} (decreases amplitude). Of particular interest though is the amplitude increase on day 7 in cells 150–165, which can be fitted by increasing the κ by ~10% (Figure 9b). Application of the empirical model (Figure 9) suggests that at low (~2%) saturation, the load-bearing form could locally increase the system κ.

5. Discussion

Similar to the *Davis et al*. [2010] experiment, *Kwon and Ajo-Franklin* [2013] conducted experiments which involved stimulating the production of the biopolymer dextran inside a column of sand and monitoring changes in κ and the seismic response using the ultrasonic pulse transmission method. Like *Davis et al*. [2010], *Kwon and Ajo-Franklin* [2013] also observed increased attenuation in conjunction with decreased κ. *Davis et al*. [2010] speculated that attenuation could have occurred due to squirt flow and scattering, whereas *Kwon and Ajo-Franklin* [2013] related the attenuation to a flow-induced loss mechanism related to the combined grain/biopolymer structure. We have presented two models for attenuation, which is by no means an exhaustive investigation but offer new insights into the system dynamics. The sparse nature of experimental data available on biofilm fundamental properties such as K, G, α, ϕ^*, and η limits model testing and development. We emphasize on the importance of a standardized method for collecting these data by the wider biofilm community.

In the *Davis et al*. [2010] experiment, except at a few sampling locations, the attenuation increased by up to ~80%. On the other hand, arrival times only increased and decreased by ~2%. This should not be interpreted as V_P being insensitive to biofilm growth. Traveltime is a kinematic property which depends on medium velocity. The medium velocity, in principle, only depends on bulk composition which should be independent of acquisition setup. Amplitude, on the other hand, is a more dynamic property. Besides the bulk composition, it also depends on acquisition setup and scale of investigation. The relative changes in amplitudes and traveltimes are also a function of the scale of sampling and the dominant frequency. For example, if the same experiment was done at a larger spatial scale, perturbations in arrival time could be better observed. Similarly, if the dominant frequency was in the sonic range (30–100 Hz), attenuation may not have been as prominent.

A close inspection of the *Davis et al*. [2010] data also suggests that in general, arrival times have spatial dependence while amplitudes have temporal dependence [*Al-Hadrami*, 2013]. We were unable to identify any strict patterns in time-lapse S_{bf}. In our opinion, for scaling this experiment to field scale, such as for CO_2 sequestration or MEOR, it will be critical to (a) acquire data in a time-lapse manner and (b) use all attributes of data along with their potential spatial and temporal patterns. Achieving repeatability in seismic experiments in field setting has its own challenges. On a related note, the model in this paper also predicts the shear-wave velocity (V_S), which could be easily acquired in the field settings. If present, V_S could additionally constrain S_{bf}.

The environmental scanning electron microscope (ESEM) images acquired at the end of the *Davis et al*. [2010] experiment (Figure 1) in zones of decreasing and increasing amplitudes corresponds to cells 20 (pore filling) and 170 (load bearing), respectively, in our model. *Davis et al*. [2010] noted that during ESEM imaging of

the zone with increasing amplitudes, the bacterial cells were not visible until the operating temperature and relative humidity were changed from 5°C to 20°C and 89% to 14%, which effectively led to drying out of the biomaterial. We interpret this as the biofilm in the increased amplitude zone to be having higher internal ϕ which is in line with our squirt flow model. The surface texture of the biofilm in this zone was vuggy with elongated crevasses. In contrast, biofilm from the decreased amplitude zone was clearly visible at 5°C operating temperature and 89% relative humidity and had relatively smoother texture and better defined pores. A higher value for α in the case of increased amplitude zone is probably reflective of the observed texture.

The empirical model result suggests that the A^{P2P} increase on day 5 is due to the local increase in κ, which occurs at low (<5%) S_{bf} in the load-bearing form. To explain this, we propose formation of "biotubes," which we envision as channels within biofilms that lead to an overall elevated hydraulic conductivity [e.g., *Stoodley et al*., 1994]. The term "tube" is to reflect the rod-shaped nature of *P. aeruginosa* bacteria. Elevated hydraulic conductivity has also been reported for other biofilms such as *Bacillus mojavensis* [*Vogt et al*., 2013] and *Bacillus subtilis* [*Wilking et al*., 2013]. We are uncertain of the exact nature of the proposed biotubes in the *Davis et al*. [2010] experiment but we hypothesize that biochanneling is concurrent with limited vertical accommodation space (Figure 6c), which automatically implies that pore throat size could affect biofilm morphology.

Fully mature *P. aeruginosa* biofilms conceptually appear as mushroom-shaped projections extending away from the surface (Figure 6c) with a texture characterized by channels and caverns [*Klausen et al*., 2003a, 2003b; *Miller et al*., 2012]. This morphology assumes unrestricted growth space and is similar to the pore-filling form in our model. It also has a more common occurrence that the load-bearing form, which is somewhat rarely reported [e.g., *Abdel-Aal et al*., 2010]. However, corroborating studies suggest that the material properties of biofilms are dynamic and shape change can occur in response to mechanical pressure [*Alpkvist and Klapper*, 2007], nutrient supply [*Chang and Halverson*, 2003], and osmotic pressure [*Seminara et al*., 2012]. We speculate that between the two mineral grains, it is the increased shear pressure due to growth which changes the biofilm structure. This is in line with *Mukherjee et al*. [2009] who suggest that shear stress can change the biofilm morphology to a thinner and denser state.

Both *Davis et al*. [2010] and *Kwon and Ajo-Franklin* [2013] observed that the amplitude decrease stops at ~80%. This phenomenon can be understood using equation (13) which implies that when ϕ and κ fall below a minimum threshold, attenuation depends on the system constants (a_0, a_4, and D). In the *Kwon and Ajo-Franklin* [2013] experiment since the size of the sand pack (as well as ϕ_0 due to grain packing) remains the same as in the *Davis et al*. [2010] experiment, the maximum attenuation is similar. The decrease in ϕ in the *Kwon and Ajo-Franklin* [2013] model is less than that predicted by our model (~6% versus ~10%), which could be due to the differences in the elastic properties of the bacteria which were cultivated in the two experiments.

Kwon and Ajo-Franklin [2013] also measured time-lapse changes in κ as decreasing from 5.25 D to 225 mD, which is very close to κ predicted by our pore-filling model (black line; Figure 9b). However, *Kwon and Ajo-Franklin* [2013] did not report any increase in κ, but it may not be inconsistent with our model. On a closer examination, the relative amplitude displayed in Figure 9a from *Kwon and Ajo-Franklin* [2013] does show that the amplitude increased on the second observation day. The similarity in the two data sets indicates that biotube-type features could be forming in the *Kwon and Ajo-Franklin* [2013] experiment as well. However, we acknowledge that more experimental data are needed for proper calibration of rock physics models to test the biotube hypothesis. Although biofilm monitoring experiments using geophysical techniques remain a challenge, such efforts could be rewarding in the long run.

6. Conclusions

We report here a pioneering effort in developing mechanistic models for biofilm growth in porous media. We show that acoustic amplitudes and arrival times recorded in a 29 day long physical scale experiment by *Davis et al*. [2010] can be modeled using the lower Hashin-Shtrikman bounds for grain mixing and Gassmann substitution for fluid saturation. Model application suggests the occurrence of two distinct biofilm forms which could form as a function of pore throat size. An increase in V_P can be explained by the biofilm load-

bearing form (in the matrix), which could occur when the vertical accommodation space is low. As a result, the biofilm bridge adjoining mineral grains expand along the grain surface and possibly interconnect. A decrease in V_P can be explained by biofilms in the pore-filling form (in the pore), which could occur when the vertical accommodation space is unrestricted. Mapping time-lapse V_P to S_{bf} suggests that overall ϕ could have decreased by 10%, with the decrease being as much as 15% at a few selected locations. Amplitude decay can be explained equally well by a deterministic squirt flow model and an empirical model as a function of ϕ and κ. Results from the squirt model suggest that the load-bearing form has higher (7% versus 5%) internal porosity and lower (0.33 versus 0.67) pore aspect ratio as compared to the pore-filling forms. Results from the empirical model suggest that local κ increases by 10% at low (~2%) S_{bf} in the load-bearing form and that a limiting threshold of 80% decrease in amplitudes is due to the grain size of the sand pack. Models developed in this paper can be applied to field seismic data by adapting them appropriate to lower frequencies and larger length scales such as will be needed for MEOR studies and biobarrier monitoring associated with CO_2 sequestration.

Acknowledgments

Seismic data used in the model development were acquired by C. Davis as part of her PhD dissertation using instrumentation in L. Pyrak-Nolte's Laboratory at Purdue University. The initial models for V_P were explored by Mouin Al-Massodi. F. Al-Hadrami was supported by Exxon Mobil. Pride Abongwa helped in geochemical modeling in section 4. This is Oklahoma State University Boone Pickens School of Geology contribution 2014-10.

References

Abdel-Aal, G., E. Atekwana, S. Radzikowski, and S. Rossbach (2009), Effect of bacterial adsorption on low frequency electrical properties of clean quartz sands and iron-oxide coated sands, *Geophys. Res. Lett.*, *36*, L04403, doi:10.1029/2008GL036196.

Abdel-Aal, G., E. A. Atekwana, and E. A. Atekwana (2010), Effect of bioclogging in porous media on complex conductivity signatures, *J. Geophys. Res.*, *115*, G00G07, doi:10.1029/2009JG001159.

Adam, L., M. Batzle, K. T. Lewallen, and K. van Wijk (2009), Seismic wave attenuation in carbonates, *J. Geophys. Res.*, *114*, B06208, doi:10.1029/2008JB005890.

Aggarwal, S., and R. M. Hozalski (2010), Determination of biofilm mechanical properties from tensile tests performed using a micro-cantilever method, *Biofouling*, *26*(4), 479–486.

Al-Hadrami, F. (2013), *Quantitative Interpretation of Bio-seismic Response*, Oklahoma State Univ., Stillwater, Okla.

Alpkvist, E., and I. Klapper (2007), Description of mechanical response including detachment using a novel particle model of biofilm/flow interaction, *Water Sci. Technol.*, *55*(8–9), 265–273.

Atekwana, E. A., and L. D. Slater (2009), Biogeophysics: A new frontier in Earth science research, *Rev. Geophys.*, *47*, RG4004, doi:10.1029/2009RG000285.

Batzle, M. L., and Z. Wang (1992), Seismic properties of pore fluids, *Geophysics*, *57*(11), 1396–1408.

Batzle, M., R. Hofmann, M. Prasad, G. Kumar, L. Duranti, and D. H. Han (2005), Seismic attenuation: Observations and mechanisms, in *SEG Technical Program Expanded Abstracts*, edited, pp. 1565-1568, Society of Exploration Geophysicists, Tulsa, Okla.

Boadu, F. K. (1997), Rock properties and seismic attenuation: Neural network analysis, *Pure Appl. Geophys.*, *149*(3), 507–524.

Chang, W.-S., and L. J. Halverson (2003), Reduced water availability influences the dynamics, development, and ultrastructural properties of Pseudomonas putida biofilms, *J. Bacteriol.*, *185*(20), 6199–6294.

Cheng, Z. D., J. X. Zhu, P. M. Chaikin, S. E. Phan, and W. B. Russel (2002), Nature of the divergence in low shear viscosity of colloidal hard-sphere dispersions, *Phys. Rev. E*, *65*(4), 8.

Costa, A. (2006), Permeability-porosity relationship: A reexamination of the Kozeny-Carman equation based on a fractal pore-space geometry assumption, *Geophys. Res. Lett.*, *33*, L02318, doi:10.1029/2005GL025134.

Cunningham, A. B., W. G. Characklis, F. Abedeen, and D. Crawford (1991), Influence of biofilm accumulation on porous-media hydrodynamics, *Environ. Sci. Technol.*, *25*(7), 1305–1311.

Davis, C. A., L. J. Pyrak-Nolte, E. A. Atekwana, D. D. Werkema, and M. E. Haugen (2010), Acoustic and electrical property changes due to microbial growth and biofilm formation in porous media, *J. Geophys. Res.*, *115*, G00G06, doi:10.1029/2009JG001143.

Davit, Y., G. Iltis, G. Debenest, S. Veran-Tissoires, D. Wildenschild, M. Gerino, and M. Quintard (2011), Imaging biofilm in porous media using X-ray computed microtomography, *J. Microsc.*, *242*(1), 15–25.

DeJong, J. T., B. M. Mortensen, B. C. Martinez, and D. C. Nelson (2010), Bio-mediated soil improvement, *Ecol. Eng.*, *36*(2), 197–210.

Drescher, K., Y. Shen, B. L. Bassler, and H. A. Stone (2013), Biofilm streamers cause catastrophic disruption of flow with consequences for environmental and medical systems, *Proc. Natl. Acad. Sci. U.S.A.*, *110*(11), 4345–4350.

Dvorkin, J., and A. Nur (1996), Elasticity of high-porosity sandstones: Theory for two North Sea data sets, *Geophysics*, *61*(5), 1363–1370.

Ehrnrooth, E. M. L. (1984), Change in pulp fibre density with acid-chlorite delignification, *J. Wood Chem. Technol.*, *4*(1), 91–109, doi:10.1080/02773818408062285.

Garcia-Betancur, J., A. Yepes, J. Schneider, and D. Lopez (2012), Single-cell analysis of Bacillus subtilis biofilms using fluorescence microscopy and flow cytometry, *J. Vis. Exp.*, *60*, e3796.

Gassmann, F. (1951), Elastic waves through a packing of spheres, *Geophysics*, *16*(4), 673–685.

Gibson, L. J. (2012), The hierarchical structure and mechanics of plant materials, *J. R. Soc. Interface*, *76*(9), 2749–2766.

Guhados, G., W. K. Wan, and J. L. Hutter (2005), Measurement of the elastic modulus of single bacterial cellulose fibers using atomic force microscopy, *Langmuir*, *21*(14), 6642–6646.

Gurevich, B., D. Makarynska, O. B. de Paula, and M. Pervukhina (2010), A simple model for squirt-flow dispersion and attenuation in fluid-saturated granular rocks, *Geophysics*, *75*(6), N109–N120.

Hall-Stoodley, L., J. W. Costerton, and P. Stoodley (2004), Bacterial biofilms: From the natural environment to infectious diseases, *Nat. Rev. Micro.*, *2*(2), 95–108.

Hill, A. R. (1952), The elastic behaviour of a crystalline aggregate, in *Proceedings of the Physical Society*, *65*(5), doi:10.1088/0370-1298/65/5/307.

Hofmann, R. (2006), *Frequency Dependent Elastic and Anelastic Properties of Clastic Rocks*, Colorado School of Mines, Golden, Colo.

Hsieh, Y.-C., H. Yano, M. Nogi, and S. J. Eichhorn (2008), *An Estimation of the Young's Modulus of Bacterial Cellulose Filaments*, Springer Science + Business Media, Netherlands.

Kasi, M., J. McEvoy, G. Padmanabhan, and E. Khan (2011), Groundwater remediation using an enricher reactor-permeable reactive biobarrier for periodically absent contaminants, *Water Environ. Res.*, *83*(7), 603–612.

Klausen, M., A. Aaes-Jørgensen, S. Molin, and T. Tolker-Nielsen (2003a), Involvement of bacterial migration in the development of complex multicellular structures in Pseudomonas aeruginosa biofilms, *Mol. Microbiol.*, *50*(1), 61–68.
Klausen, M., A. Heydorn, P. Ragas, L. Lambertsen, A. Aaes-Jorgensen, S. Molin, and T. Tolker-Nielsen (2003b), Biofilm formation by Pseudomonas aeruginosa wild type, flagella and type IV pili mutants, *Mol. Microbiol.*, *48*(6), 1511–1524.
Konhauser, K. O., and M. K. Gingras (2007), Linking geomicrobiology with ichnology in marine sediments, *Palaios*, *22*(4), 339–342.
Kwon, T., and J. Ajo-Franklin (2013), High-frequency seismic response during permeability reduction due to biopolymer clogging in unconsolidated porous media, *Geophysics*, *78*(6), EN117–EN127.
Lawrence, J. R., and T. R. Neu (1999), Confocal laser scanning microscopy for analysis of microbial biofilms, in *Methods in Enzymology*, edited by J. D. Ron, pp. 131–144, Academic Press Elsevier Inc., Amsterdam.
Lazar, I., I. G. Petrisor, and T. F. Yen (2007), Microbial Enhanced Oil Recovery (MEOR), *Pet. Sci. Technol.*, *25*(11), 1353–1366.
Le Chatelier, H. (1998), Limits of flammability of gaseous mixtures, *Bull. Soc. Chim. Fr.*, *19*, 483–488.
Lear, G., and G. Lewis (2012), *Microbial Biofilms: Current Research and Applications*, Caister Academic Press, Norwich, U. K.
Li, X., and L. J. Pyrak-Nolte (1998), Acoustic monitoring of sediment-pore fluid interaction, *Geophys. Res. Lett.*, *25*(20), 3899–3902, doi:10.1029/1998GL900028.
Manz, B., F. Volke, D. Goll, and H. Horn (2003), Measuring local flow velocities and biofilm structure in biofilm systems with magnetic resonance imaging (MRI), *Biotechnol. Bioeng.*, *84*, 424–432.
Mavko, G. M., and A. Nur (1979), Wave attenuation in partially saturated rocks, *Geophysics*, *44*(2), 161–178.
Mavko, G., and R. Nolen-Hoeksema (1994), Estimating seismic velocities at ultrasonic frequencies in partially saturated rocks, *Geophysics*, *59*(2), 252–258.
Mavko, G., T. Mukerji, and J. Dvorkin (2009), *The Rock Physics Handbook*, 2nd ed., Cambridge Univ. Press, Cambridge, England.
Miller, J. K., H. T. Badawy, C. Clemons, K. L. Kreider, P. Wilber, A. Milsted, and G. Young (2012), Development of the Pseudomonas aeruginosa mushroom morphology and cavity formation by iron-starvation: A mathematical modeling study, *J. Theor. Biol.*, *308*(0), 68-78.
Mindlin, R. D. (1949), Compliance of elastic bodies in contact, *J. Appl. Mech.-Trans. ASME*, *16*(3), 259–268.
Mitchell, A. C., K. Dideriksen, L. H. Spangler, A. B. Cunningham, and R. Gerlach (2010), Microbially enhanced carbon capture and storage by mineral-trapping and solubility-trapping, *Environ. Sci. Technol.*, *44*(13), 5270–5276.
Mukherjee, P. K., D. V. Chand, J. Chandra, J. M. Anderson, and M. A. Ghannoum (2009), Shear stress modulates the thickness and architecture of Candida albicans biofilms in a phase-dependent manner, *Mycoses*, *52*(5), 440–446.
Nishi, Y., M. Uryu, S. Yamanaka, K. Watanabe, N. Kitamura, M. Iguchi, and S. Mitsuhashi (1990), The structure and mechanical-properties of sheets prepared from bacterial cellulose. 2. Improvement of the mechanical-properties of sheets and their applicability to diaphragms of electroacoustic transducers, *J. Mater. Sci.*, *25*(6), 2997–3001.
Nolen-Hoeksema, R. C. (2000), Modulus–porosity relations, Gassmann's equations, and the low-frequency elastic-wave response to fluids, *Geophysics*, *65*(5), 1355–1363.
Rabah, F. K. J., and M. F. Dahab (2004), Biofilm and biomass characteristics in high-performance fluidized-bed biofilm reactors, *Water Res.*, *38*(19), 4262–4270.
Rosenzweig, R., A. Furman, and U. Shavit (2013), A channel network model as a framework for characterizing variably saturated flow in biofilm-affected soils, *Gsvadzone*, *12*, 2, doi:10.2136/vzj2012.0079.
Seifert, D., and P. Engesgaard (2007), Use of tracer tests to investigate changes in flow and transport properties due to bioclogging of porous media, *J. Contam. Hydrol.*, *93*(1–4), 58–71.
Seminara, A., T. E. Angelini, J. N. Wilking, H. Vlamakis, S. Ebrahim, R. Kolter, D. A. Weitz, and M. P. Brenner (2012), Osmotic spreading of Bacillus subtilis biofilms driven by an extracellular matrix, *Proc. Natl. Acad. Sci. U.S.A.*, *109*(4), 1116–1121.
Sloan, D. E., and C. A. Koh (2008), *Clathrate Hydrate of Natural Gases*, 3rd ed., CRC Press, Boca Raton, Fla.
Smith, F. L., and A. H. Harvey (2007), Avoid common pitfalls when using Henry's law, *Chem. Eng. Prog.*, *103*(9), 33–39.
Stoodley, P., D. DeBeer, and Z. Lewandowski (1994), Liquid flow in biofilm systems, *Appl. Environ. Microbiol.*, *60*(8), 2711–2716.
Stoodley, P., Z. Lewandowski, J. D. Boyle, and H. M. Lappin-Scott (1998), Oscillation characteristics of biofilm streamers in turbulent flowing water as related to drag and pressure drop, *Biotechnol. Bioeng.*, *57*(5), 536–544.
Stoodley, P., R. Cargo, C. J. Rupp, S. Wilson, and I. Klapper (2002), Biofilm material properties as related to shear-induced deformation and detachment phenomena, *J. Ind. Microbiol. Biotechnol.*, *29*(6), 361–367.
Tajima, K., M. Fujiwara, and M. Takai (1995), Biological control of cellulose, *Macromol. Symp.*, *99*, 149–155.
Talukdar, M. M., I. Vinckier, P. Moldenaers, and R. Kinget (1996), Rheological characterization of xanthan gum and hydroxypropylmethyl cellulose with respect to controlled-release drug delivery, *J. Pharm. Sci.*, *85*(5), 537–540.
Taylor, S. W., and P. R. Jaffé (1990), Biofilm growth and the related changes in the physical properties of a porous medium: 3. Dispersivity and model verification, *Water Resour. Res.*, *26*, 2171–2180, doi:10.1029/WR026i009p02171.
Vogt, S., A. B. Sanderlin, J. D. Seymour, and S. L. Codd (2013), Permeability of a growing biofilm in a porous media fluid flow analyzed by magnetic resonance displacement-relaxation correlations, *Biotechnol. Bioeng.*, *110*, 1366–1375.
Wilking, J. N., T. E. Angelini, A. Seminara, M. P. Brenner, and D. A. Weitz (2011), Biofilms as complex fluids, *MRS Bull.*, *36*(05), 385–391.
Wilking, J. N., V. Zaburdaev, M. De Volder, R. Losick, M. P. Brenner, and D. A. Weitz (2013), Liquid transport facilitated by channels in Bacillus subtilis biofilms, *Proc. Natl. Acad. Sci. U.S.A.*, *110*(3), 848–852.
Williams, K. H., D. Ntarlagiannis, L. D. Slater, A. Dohnalkova, S. S. Hubbard, and J. F. Banfield (2005), Geophysical imaging of stimulated microbial biomineralization, *Environ. Sci. Technol.*, *39*(19), 7592–7600.
Xu, S. Y., and R. E. White (1995), A new velocity model for clay-sand mixtures, *Geophys. Prospect.*, *43*(1), 91–118.
Zhang, T. C., and P. L. Bishop (1994), Density, porosity, and pore structure of biofilms, *Water Res.*, *28*(11), 2267–2277.